

REPORT DOCUMENTATION PAGE				Form Approved OMB NO. 0704-0188	
<p>The public reporting burden for this collection of information is estimated to average 1 hour per response, including the time for reviewing instructions, searching existing data sources, gathering and maintaining the data needed, and completing and reviewing the collection of information. Send comments regarding this burden estimate or any other aspect of this collection of information, including suggestions for reducing this burden, to Washington Headquarters Services, Directorate for Information Operations and Reports, 1215 Jefferson Davis Highway, Suite 1204, Arlington VA, 22202-4302. Respondents should be aware that notwithstanding any other provision of law, no person shall be subject to any penalty for failing to comply with a collection of information if it does not display a currently valid OMB control number.</p> <p>PLEASE DO NOT RETURN YOUR FORM TO THE ABOVE ADDRESS.</p>					
1. REPORT DATE (DD-MM-YYYY)		2. REPORT TYPE		3. DATES COVERED (From - To)	
		New Reprint		-	
4. TITLE AND SUBTITLE Joint diagonalization applied to the detection and discrimination of unexploded ordnance				5a. CONTRACT NUMBER	
				W911NF-08-1-0385	
				5b. GRANT NUMBER	
				5c. PROGRAM ELEMENT NUMBER	
6. AUTHORS Fridon Shubitidze, Juan Pablo Fernandez, Irma Shamatava, Benjamin E. Barrowes, Kevin O'Neill				5d. PROJECT NUMBER	
				5e. TASK NUMBER	
				5f. WORK UNIT NUMBER	
7. PERFORMING ORGANIZATION NAMES AND ADDRESSES Dartmouth College Office of Sponsored Projects Trustees of Dartmouth College Hanover, NH 03753 -1404				8. PERFORMING ORGANIZATION REPORT NUMBER	
9. SPONSORING/MONITORING AGENCY NAME(S) AND ADDRESS(ES) U.S. Army Research Office P.O. Box 12211 Research Triangle Park, NC 27709-2211				10. SPONSOR/MONITOR'S ACRONYM(S) ARO	
				11. SPONSOR/MONITOR'S REPORT NUMBER(S) 55000-EV.3	
12. DISTRIBUTION AVAILABILITY STATEMENT Approved for public release; distribution is unlimited.					
13. SUPPLEMENTARY NOTES The views, opinions and/or findings contained in this report are those of the author(s) and should not be construed as an official Department of the Army position, policy or decision, unless so designated by other documentation.					
14. ABSTRACT Efforts to discriminate buried unexploded ordnance from harmless surrounding clutter are often hampered by the uncertainty in the number of buried targets that produce a given detected signal. We present a technique that helps determine that number with no need for data inversion. The procedure is based on the joint diagonalization of a set of multistatic response (MSR) matrices measured at different time gates by a time-domain electromagnetic induction sensor. In particular, we consider the Naval Research Laboratory's Time-Domain Electromagnetic					
15. SUBJECT TERMS UXO, Joint diagonalization					
16. SECURITY CLASSIFICATION OF:			17. LIMITATION OF ABSTRACT	15. NUMBER OF PAGES	19a. NAME OF RESPONSIBLE PERSON
a. REPORT	b. ABSTRACT	c. THIS PAGE			Fridon Shubitidze
UU	UU	UU	UU		19b. TELEPHONE NUMBER
					603-646-3671

Report Title

Joint diagonalization applied to the detection and discrimination of unexploded ordnance

ABSTRACT

Efforts to discriminate buried unexploded ordnance from harmless surrounding clutter are often hampered by the uncertainty in the number of buried targets that produce a given detected signal. We present a technique that helps determine that number with no need for data inversion. The procedure is based on the joint diagonalization of a set of multistatic response (MSR) matrices measured at different time gates by a time-domain electromagnetic induction sensor. In particular, we consider the Naval Research Laboratory's Time-Domain Electromagnetic Multisensor Towed Array Detection System (TEMTADS), which consists of a 5×5 square grid of concentric transmitter/receiver pairs. The diagonalization process itself generalizes one of the standard procedures for extracting the eigenvalues of a single matrix; in terms of execution time, it is comparable to diagonalizing the matrices one by one. We present the method, discuss and illustrate its mathematical basis and physical meaning, and apply it to several actual measurements carried out with TEMTADS at a test stand and in the field at the former Camp Butner in North Carolina. We find that each target in a measurement is associated with a set of nonzero time-dependent MSR eigenvalues (usually three), which enables estimation of the number of targets interrogated. These eigenvalues have a characteristic shape as a function of time that does not change with the location and orientation of the target relative to the sensor. We justify analytically and empirically that symmetric targets have pairs of eigenvalues with constant ratios between them

REPORT DOCUMENTATION PAGE (SF298)
(Continuation Sheet)

Continuation for Block 13

ARO Report Number 55000.3-EV

Joint diagonalization applied to the detection and ...

Block 13: Supplementary Note

© 2012 . Published in Geophysics, Vol. Ed. 0 77, (4) (2012), (, (4). DoD Components reserve a royalty-free, nonexclusive and irrevocable right to reproduce, publish, or otherwise use the work for Federal purposes, and to authroize others to do so (DODGARS §32.36). The views, opinions and/or findings contained in this report are those of the author(s) and should not be construed as an official Department of the Army position, policy or decision, unless so designated by other documentation.

Approved for public release; distribution is unlimited.

Joint diagonalization applied to the detection and discrimination of unexploded ordnance

Fridon Shubitidze¹, Juan Pablo Fernández², Irma Shamatava¹, Benjamin E. Barrowes³, and Kevin O'Neill³

ABSTRACT

Efforts to discriminate buried unexploded ordnance from harmless surrounding clutter are often hampered by the uncertainty in the number of buried targets that produce a given detected signal. We present a technique that helps determine that number with no need for data inversion. The procedure is based on the joint diagonalization of a set of multistatic response (MSR) matrices measured at different time gates by a time-domain electromagnetic induction sensor. In particular, we consider the Naval Research Laboratory's Time-Domain Electromagnetic Multisensor Towed Array Detection System (TEMTADS), which consists of a 5×5 square grid of concentric transmitter/receiver pairs. The diagonalization process itself generalizes one of the standard procedures for extracting

the eigenvalues of a single matrix; in terms of execution time, it is comparable to diagonalizing the matrices one by one. We present the method, discuss and illustrate its mathematical basis and physical meaning, and apply it to several actual measurements carried out with TEMTADS at a test stand and in the field at the former Camp Butner in North Carolina. We find that each target in a measurement is associated with a set of nonzero time-dependent MSR eigenvalues (usually three), which enables estimation of the number of targets interrogated. These eigenvalues have a characteristic shape as a function of time that does not change with the location and orientation of the target relative to the sensor. We justify analytically and empirically that symmetric targets have pairs of eigenvalues with constant ratios between them.

INTRODUCTION

The United States military has identified as one of its main environmental challenges reducing the worldwide profusion of unexploded ordnance (UXO) contaminating former military training grounds and battle-scarred territory. UXO kill or maim more people in conflict zones each year than do landmines (Moyes et al., 2002); they also cause frequent disruption in nations at peace. Remediation of UXO-tainted land is laborious and expensive: targets of interest are usually surrounded by metallic clutter, natural and artificial, that is also detected by sensors, and in some areas, the targets themselves are also densely clustered. Thus, it is often not clear how many buried targets contribute to a given detected signal, or how

many are dangerous, and this shortage of information complicates identification attempts. This paper aims to ease UXO remediation by presenting a method to estimate the number of targets and thus assess scene complexity quickly and reliably on the basis of electromagnetic induction (EMI) data.

In EMI sensing, a time-dependent primary magnetic field established by a sensor induces eddy currents and/or magnetic domain realignments in nearby ferrous and nonferrous metallic objects. This response, in turn, gives rise to a measurable secondary magnetic field. The measured signal, often referred to as an "anomaly" detected at a "cell," depends on the sizes, shapes, and material properties of the targets under interrogation and also on the particulars of the measurement, i.e., the relative distances and attitudes

Manuscript received by the Editor 3 October 2011; revised manuscript received 16 April 2012; published online 9 July 2012.

¹Thayer School of Engineering, Dartmouth College, Hanover, New Hampshire, USA and Sky Research, Inc., Etna, New Hampshire, USA. E-mail: fridon.shubitidze@dartmouth.edu; irma.shamatava@dartmouth.edu.

²88 Franklin St. Unit 301, Lynn, Massachusetts 01902-4171, USA. E-mail: jpf@alumni.umass.edu.

³Thayer School of Engineering, Dartmouth College, Hanover, New Hampshire, USA and U.S. Army Corps of Engineers, ERDC-CRREL, Hanover, New Hampshire, USA. E-mail: benjamin.e.barrowes@usace.army.mil; kevin.o'neill@usace.army.mil.

© 2012 Society of Exploration Geophysicists. All rights reserved.

between the targets and the sensor. The main task of the data analysis is to separate these “intrinsic” and “extrinsic” factors to determine what targets are producing the anomaly and where and how deep they are within the cell. This inverse problem is usually solved using a combination of linear and nonlinear least squares to fit a model to the measurements (Aster et al., 2005; Everett, 2012).

Several models used with success to detect and characterize buried metal targets build on the premise that the currents and domains that generate electromagnetic response are not distributed uniformly within each target, but instead, tend to concentrate around certain singular points or regions. The techniques synthesize that response as though it consisted of a set of analytic solutions of the Maxwell equations due to point sources located at those so-called “scattered field singularities” (Bogdanov et al., 1999; Karkashadze et al., 2009). The time-dependent behavior of these sources is used to characterize and classify the causative targets. (In this work, we use “source” to refer to these elementary analytic solutions, and not, as is often the case in geophysics, to transmitters.)

The number of scattered field singularities depends on the wavelength and on the scatterers’ geometry and material properties. In the EMI frequency regime, where the wavelengths are significantly larger than the targets’ characteristic lengths, most homogeneous compact targets have a dominant singularity at their centers. Therefore, the simplest and most widely used approach replaces each target with a single point magnetic dipole located near its geometric center (Das et al., 1990; Barrow and Nelson, 2001; Bell et al., 2001; Pasion and Oldenburg, 2001; Zhang et al., 2003; Smith and Morrison, 2004; Tarokh et al., 2004; Fernández et al., 2011). This point dipole model tends to work best for relatively small and distant targets, and in terms of predictive accuracy and consistency has been superseded by generalizations that distribute dipole-moment densities over surfaces or volumes (Shubitidze et al., 2010b, 2010c). On the other hand, all of these models fare less well when analyzing anomalies due to more than one target: The inversion becomes more computationally expensive, has more local minima, and may require regularization (Song et al., 2009, 2011; Grzegorzczak et al., 2011). When the number of targets is not known a priori, as in all real-world tests, the situation is complicated further because the models must be run several times (assuming different target numbers) and have the tendency to overfit the data.

The approach we introduce here is designed to make a fast estimate of the number of targets in a cell. It is not meant to replace actual inversion because it does not yield location information and does not characterize targets with complete precision, but rather constitutes an initial pre-inversion step. (The inversion routines that use as input the resulting number estimates are presented elsewhere (Shubitidze et al., 2010a, 2010b) and will be studied in detail in a companion paper.)

The technique is based on the joint diagonalization (JD) of a sequence of square time-dependent multistatic response (MSR) matrices that are synthesized directly from measured EMI signals without invoking a forward model. The number of nonzero time-dependent eigenvalues of the set of matrices is related to the number of meaningful elementary sources present in the illuminated cell. As will be shown in the “Methods” section, a single source generating three eigenvalues may suffice to describe a small or deeply buried target. A complex field structure, caused by a large, heterogeneous, or very shallow target, may require more than one elementary source (and thus more than three time-dependent eigenvalues) to

describe the resulting field adequately. Objects like thin wires or rings that are “small” along one or more dimensions may require less than three time-dependent eigenvalues.

Joint diagonalization has become an important tool for signal processing and inverse problems, including independent component analysis (Comon, 1994), blind source separation (BSS) (Belouchrani et al., 1997), common principal component analysis, and kernel-based nonlinear BSS (Harmeling et al., 2003). To the best of our knowledge, this is the first use of this technique for UXO discrimination.

METHODS

The TEMTADS sensor array

EMI sensors operate at very low frequencies (a few Hz to a few hundred kHz) to penetrate conductive ground, resulting in data with poor spatial resolution. Advanced EMI sensors have been designed to overcome this limitation: They enhance the information content of the data by increasing the number of sensor/target attitudes and reduce positioning uncertainty by employing rigid arrays of transmitters and receivers. One such instrument is the Time-domain Electromagnetic Multisensor Towed Array Detection System (TEMTADS), developed by the Naval Research Laboratory and G&G Sciences, Inc. (Steinhurst et al., 2010), to which we restrict attention.

Shown in Figure 1, TEMTADS is a time-domain EMI sensor that consists of 25 transmitter/receiver (Tx/Rx) pairs, each composed of a 35-cm square transmitter loop surrounding a 25-cm square receiver loop. The Tx/Rx pairs are arrayed as a rectangular 5×5 grid with 40-cm neighbor-to-neighbor separation for a total array dimension of 2 m. At each location, the sensor activates the transmitter loops in sequence, and for each transmission all receivers record signals, providing 625 EMI transients from $\sim 100 \mu\text{s}$ to 25 ms over $N_g = 123$ time gates.

Multistatic response matrices

To construct the MSR matrices, one assembles the 625 readings at each time gate into a 25×25 array so that each column stands for one of N_t transmitters and each row represents one of N_r receivers:

$$\mathbf{S}(t_k) = \begin{bmatrix} H_{11} & H_{12} & \cdots & H_{1N_t} \\ H_{21} & H_{22} & \cdots & H_{2N_t} \\ \vdots & \vdots & \ddots & \vdots \\ H_{N_r1} & H_{N_r2} & \cdots & H_{N_rN_t} \end{bmatrix}, \quad k = 1, \dots, N_g, \quad (1)$$

where the element H_{ij} is the field measured by the i th receiver in response to the j th transmitter. Below, we look at the time development of the MSR sequence; here, we concentrate on a single time gate and interpret the information contained in each matrix. It is shown in this paper that the measured data are resolved as a superposition of “elemental” spatio-temporal subsignals, each related to the EMI signature of an elementary magnetic dipole source. Assume there are N such sources. We postulate that the field of the j th transmitter, immediately upon being shut off, induces in the l th source a dipole moment given by

$$\mathbf{m}_{jl} = \mathbf{U}_l \mathbf{A}_l \mathbf{U}_l^T \mathbf{B}_{jl}^{\text{pr}}, \quad (2)$$

where $\mathbf{B}_{jl}^{\text{pr}}$ represents the primary magnetic induction and the Euler rotation matrix \mathbf{U}_l relates the transmitter array coordinate axes to the principal axes of the source. The diagonal polarizability matrix $\mathbf{\Lambda}_l$, intrinsic to the source, measures the strength of the moment that the primary field induces along each of the source axes. This polarizability matrix contains, in principle, all the time-dependent information in the measured secondary signal.

To compute the primary magnetic induction $\mathbf{B}_{jl}^{\text{pr}}$, recall that the TEMTADS transmitter assembly consists of coplanar square loops forming a regular grid. The Biot-Savart law prescribes the primary magnetic induction at location \mathbf{r}_l of the l th source when the j th transmitter antenna (of area σ_{Tx_j}) is excited by a current I_j :

$$\mathbf{B}_{jl}^{\text{pr}} = \frac{\mu_0 I_j}{4\pi} \sigma_{\text{Tx}_j} \oint_{\text{Tx}_j} \frac{d\mathbf{l}' \times (\mathbf{r}_l - \mathbf{r}')}{|\mathbf{r}_l - \mathbf{r}'|^3} = \mathbf{g}_{jl}^{\text{pr}} \sigma_{\text{Tx}_j} I_j, \quad (3)$$

where μ_0 is the permeability of free space, $d\mathbf{l}'$ is the usual Biot-Savart line element, and we have introduced the normalized Green function $\mathbf{g}_{jl}^{\text{pr}}$.

According to Faraday's law, the signal measured by a receiver coil is the negative time derivative of the magnetic flux passing through it. (Long enough after transmitter shut-off, this flux is purely secondary.) The field at \mathbf{r} of a dipole of moment \mathbf{m} at \mathbf{r}_l is

$$\mathbf{B} = \frac{\mu_0}{4\pi} \nabla \times \left(\mathbf{m} \times \frac{\mathbf{r} - \mathbf{r}_l}{|\mathbf{r} - \mathbf{r}_l|^3} \right), \quad \text{and thus} \\ \int \mathbf{B} \cdot d\mathbf{s} = -\mathbf{m} \cdot \frac{\mu_0}{4\pi} \oint d\mathbf{l} \times \frac{\mathbf{r} - \mathbf{r}_l}{|\mathbf{r} - \mathbf{r}_l|^3} \quad (4)$$

by straightforward application of Stokes's theorem. Thus, the signal sampled at time t_k by the i th receiver (of area σ_{Rx_i}) when the i th source is excited by the j th transmitter is

$$H_{ij}^i(t_k) \sigma_{\text{Rx}_i} \sigma_{\text{Tx}_j} I_j = \frac{\mu_0}{4\pi} \sigma_{\text{Rx}_i} \frac{1}{\sigma_{\text{Rx}_i}} \oint_{\text{Rx}_i} \frac{d\mathbf{l}' \times (\mathbf{r}' - \mathbf{r}_l)}{|\mathbf{r}' - \mathbf{r}_l|^3} \cdot \dot{\mathbf{m}}_{jl}(t_k) \\ = \mathbf{g}_{li}^{\text{sc}} \sigma_{\text{Rx}_i} \cdot \dot{\mathbf{m}}_{jl}(t_k) \\ = \mathbf{g}_{li}^{\text{sc}} \sigma_{\text{Rx}_i} \cdot [\mathbf{U} \dot{\mathbf{\Lambda}}_l(t_k) \mathbf{U}^T] \cdot \mathbf{g}_{jl}^{\text{pr}} \sigma_{\text{Tx}_j} I_j, \quad (5)$$

where a dot over a variable indicates its time derivative. We have also introduced the normalized Green function $\mathbf{g}_{li}^{\text{sc}}$ in analogy with $\mathbf{g}_{jl}^{\text{pr}}$; the two are seen to have the same form. In equations 4 and 5, the line element $d\mathbf{l}'$ lies on the x - y plane, and, as a consequence, the Green functions are similar in structure to those of the simple model presented in Appendix A (in which vertical dipoles establish the primary field and only the z -component of the secondary field is measured). Note that, in the definition of the received signal, we have included the exciting current I_j and the transmitter and receiver areas; these quantities are known and can be factored out.

At a given time gate, and with only the l th source present, we construct the MSR matrix for the complete transmitter/receiver array by tiling all the $N_r \times N_t$ available samples of expression 5:

$$\mathbf{S} = \mathbf{G}^{\text{sc}} \mathbf{U}_l \dot{\mathbf{\Lambda}}_l \mathbf{U}_l^T (\mathbf{G}^{\text{pr}})^T = (\mathbf{G}^{\text{sc}} \mathbf{U}_l) \dot{\mathbf{\Lambda}}_l (\mathbf{G}^{\text{pr}} \mathbf{U}_l)^T, \quad (6)$$

where the primary (or transmitter) dyad \mathbf{G}^{pr} is of size $N_t \times 3$, the secondary (or receiver) dyad \mathbf{G}^{sc} is of size $N_r \times 3$, and the response matrix $\mathbf{U}_l \dot{\mathbf{\Lambda}}_l \mathbf{U}_l^T$ is 3×3 . The matrix \mathbf{S} has size $N_r \times N_t$ and is square

if $N_r = N_t$, as with TEMTADS. Moreover, the condition $\mathbf{G}_l^{\text{sc}} = \mathbf{G}_l^{\text{pr}} \equiv \mathbf{G}_l$ holds approximately even though the receivers do not coincide exactly with the transmitters. This means that the matrix can be diagonalized to yield real eigenvalues and eigenvectors. (This diagonalization is more precisely a singular value decomposition (SVD) for each time gate, and we use "diagonalization" as shorthand for "SVD of a symmetric matrix" in what follows.) Because $\mathbf{U}_l \dot{\mathbf{\Lambda}}_l \mathbf{U}_l^T$ is 3×3 , the matrix \mathbf{S} has only three nonzero eigenvalues for a single source; this property is the basis of the method. When there is more than one source present, the decomposition 6 expands to

$$\mathbf{S} = [\mathbf{G}_1^{\text{sc}} \quad \mathbf{G}_2^{\text{sc}} \quad \dots] \begin{bmatrix} \mathbf{U}_1 \dot{\mathbf{\Lambda}}_1 \mathbf{U}_1^T & 0 & \dots \\ 0 & \mathbf{U}_2 \dot{\mathbf{\Lambda}}_2 \mathbf{U}_2^T & \dots \\ \vdots & \vdots & \ddots \end{bmatrix} \begin{bmatrix} (\mathbf{G}_1^{\text{pr}})^T \\ (\mathbf{G}_2^{\text{pr}})^T \\ \vdots \end{bmatrix} \\ = [\mathbf{G}_1^{\text{sc}} \mathbf{U}_1 \quad \mathbf{G}_2^{\text{sc}} \mathbf{U}_2 \quad \dots] \begin{bmatrix} \dot{\mathbf{\Lambda}}_1 & 0 & \dots \\ 0 & \dot{\mathbf{\Lambda}}_2 & \dots \\ \vdots & \vdots & \ddots \end{bmatrix} \begin{bmatrix} (\mathbf{G}_1^{\text{pr}} \mathbf{U}_1)^T \\ (\mathbf{G}_2^{\text{pr}} \mathbf{U}_2)^T \\ \vdots \end{bmatrix}, \quad (7)$$

where again $\mathbf{G}_l^{\text{sc}} = \mathbf{G}_l^{\text{pr}} \equiv \mathbf{G}_l$. Formally, the intrinsic middle matrix in equation 7 has size $3N \times 3N$, where N is the number of sources; numerically, it is a $3N \times 3N$ block-diagonal matrix padded with zeros to reach a size of $N_r \times N_t$ and thus with only $3N$ nonzero

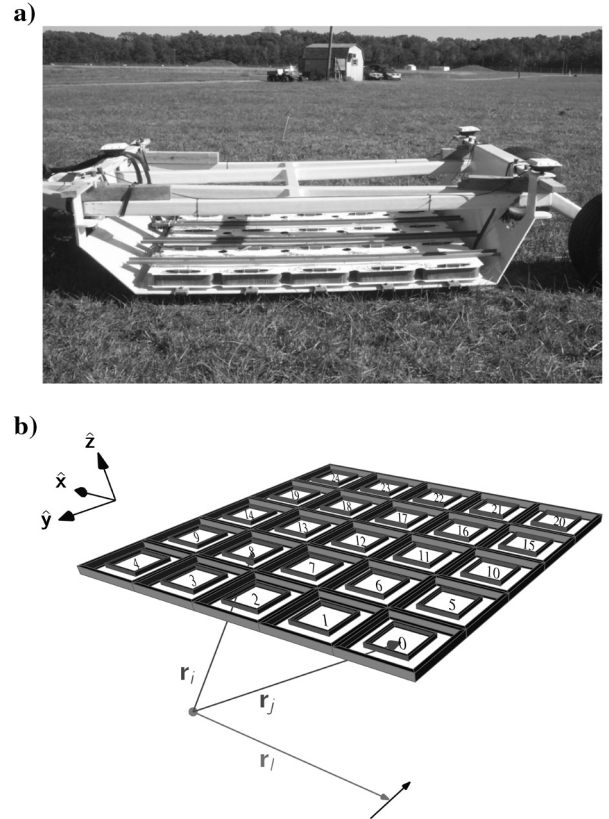


Figure 1. Photograph (a) and sketch (b) of the TEMTADS sensor array.

eigenvalues. The method should be able to resolve up to $\lfloor N_r/3 \rfloor$ responding dipole sources, or eight for TEMTADS.

This procedure would be equivalent to full inversion (though without the positional information) if one could extract directly the derivative $\dot{\mathbf{A}}$ of the polarizability matrix. This is not possible, however, because the Green dyads are not orthogonal. The actual quantities obtained from the diagonalization can be found by replacing the Green dyads by their SVDs:

$$\begin{aligned} \mathbf{S} &= \mathbf{G}\dot{\mathbf{A}}\mathbf{U}^T\mathbf{G}^T = \mathbf{W}[\Sigma\mathbf{V}^T\mathbf{U}\dot{\mathbf{A}}\mathbf{U}^T\mathbf{V}\Sigma]\mathbf{W}^T \\ &= \mathbf{W}\mathbf{Z}\mathbf{A}\mathbf{Z}^T\mathbf{W}^T = \mathbf{Y}\mathbf{A}\mathbf{Y}^T. \end{aligned} \quad (8)$$

(The matrix within brackets in the second step is real and symmetric and thus has a purely real eigendecomposition.) Equation 8 shows that the eigenvalues stored in matrix \mathbf{A} are not solely composed of source responses, but also contain location and orientation information from the Green dyads. The crucial point is that the eigenvalues contain all of the time dependence of the signal, a property that we now exploit.

Time development of the MSR eigenvalues

The second step of the procedure consists of incorporating the time dependence of the MSR matrices in the eigenvalue analysis from the previous section. As we shall see below, this information is more useful if each eigenvalue can be tracked separately as the signal decays and associated with the same time-independent eigenvector. Thus, it is necessary to diagonalize the $N_g = 123$ matrices simultaneously such that they share the same set of orthonormal time-independent eigenvectors, and these appear in the same order at all times. Denoting again as $\mathbf{S}(t_k)$ the MSR matrix at the k th time gate, a unitary matrix \mathbf{V} is sought such that the products

$$\mathbf{D}_k = \mathbf{V}^T\mathbf{S}(t_k)\mathbf{V} \quad (9)$$

are “as diagonal as possible” in the sense of definition B-1 in Appendix B. From now on, we concentrate on these time-decaying diagonal elements, referring to them as “eigenvalues” even though

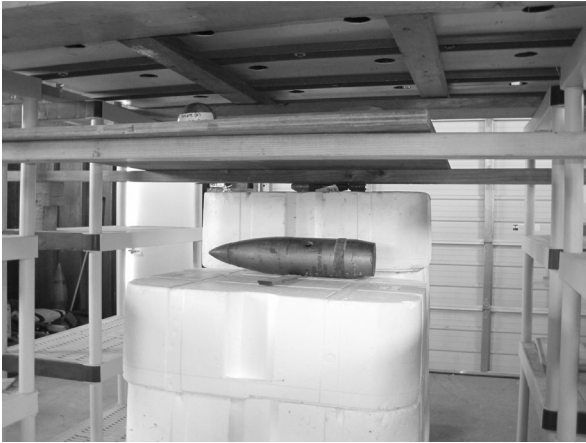


Figure 2. A test-stand experiment featuring an increasing number of targets under interrogation by TEMTADS. As in Figure 1, the system is observed essentially head-on from the $+\hat{\mathbf{y}}$ -direction.

eigenvalues are in rigor scalars, not curves, and describing them as “parallel” or “crossing each other” in a way that the figures will make clear.

One could in principle diagonalize the MSR matrix at each time gate, and the eigenvectors, which depend only on geometry, should stay constant. The fact that we cannot know a priori the order in which the eigenvalues and their corresponding eigenvectors result from each single-gate diagonalization would be only a minor complication if the data had no noise. Instead, we look for an orthogonal matrix of eigenvectors that diagonalizes all the MSR matrices simultaneously. Two different procedures, described in Appendix B, were employed with identical results. The most efficient one (Flury and Gautschi, 1986; Cardoso and Souloumiac, 1996; Belouchrani et al., 1997) is a well-known generalization of the Jacobi method for diagonalizing single matrices. We note that further development of our procedure, generalized for nonsymmetric and nonsquare MSR matrices, may require the use of a joint SVD algorithm, with two sets of shared vectors instead of one (Machara and Murota, 2011).

RESULTS

Test-stand measurements

The main purpose of the JD technique is to estimate the number of targets producing a given measured signal. In this section, we first describe an idealized experiment that was designed to act as a benchmark for multitarget scenarios while avoiding some of the complications that arise in the field. The experiment was carried out by personnel from Nova Research, Inc. on 15 January 2010. The setup is depicted in Figure 2. The TEMTADS sensor array was placed on an elevated platform. Underneath, several targets were added in sequence to form an increasingly complex scene, with the instrument measuring the response of every configuration.

The targets of interest (TOI) were two common UXO, a 105-mm M60 howitzer shell and a 60-mm mortar round. Each lay on its side with nose pointing in the $+\hat{\mathbf{x}}$ direction: the 105-mm was at a depth of 63 cm below the center of the sensor, while the 60-mm was 38 cm below the instrument and displaced 40 cm in the $-\hat{\mathbf{y}}$ -direction from the sensor center. A sphere and a spheroid were successively placed 27.5 cm below TEMTADS to simulate shallow clutter with the potential to obscure the targets of interest. The sphere, placed at $10(\hat{\mathbf{x}} + \hat{\mathbf{y}})$ cm from the origin, was made of aluminum and was 10 cm in diameter; the spheroid, made of steel with major and minor axes 20 and 4 cm, respectively, was at $-(30\hat{\mathbf{x}} + 40\hat{\mathbf{y}})$ cm from the center.

Initially, the targets were interrogated individually. Figure 3a shows the complete set of 25 eigenvalues obtained for the 105-mm shell, Figure 3b shows the same result for the 60-mm round, and Figure 4 displays the decay curves for the sphere and spheroid added in the course of the experiment. In all cases, at least three time-dependent eigenvalues emerge from the background noise. (Eigenvalues that could be associated with high-order sources such as quadrupoles are indistinguishable from the noise.) Two eigenvalues look parallel to one another (i.e., there is a constant ratio between the two); for the sphere of Figure 4a two coincide and the third is parallel. This parallelism is indicative of cylindrical symmetry, as we justify in Appendix A using a simplified model. The 60-mm round has eigenvalues of comparable size to those of the 105-mm shell, even though the target is much smaller. This is due to the fact that the eigenvalues do not store only intrinsic

responses but also positional information. It can also be noted that the 105-mm shell has at least one more above-noise eigenvalue, showing that it is not as accurately represented by a single source as the 60-mm round.

The fact that the eigenvalues change with location points out the necessity of diagonalizing the sequence of MSR matrices simultaneously. Consider the 60-mm round of Figure 3b. TEMTADS measurements were carried out on the same target at a different set of locations: Under the sensor at a depth of 35 cm (3 cm shallower than in Figure 3b), $-10(\hat{x} + \hat{y})$ cm from the center and 29.5 cm below the sensor, and at the latter depth but under the center. Figure 5 shows the eigenvalue decay curves that result from carrying out joint diagonalization on these three data sets, whereas Figure 6 shows the same decay curves computed time gate by time gate using the SVD. Both methods find three above-threshold eigenvalues and correctly predict that there is only one target, but the eigenvalues' time developments have a crucial difference: The JD eigenvalues preserve their shapes case to case, even as the relative amplitudes vary, whereas those obtained with the SVD change shape as the

object location varies. The simple sorting provided by the SVD explicitly disallows the eigenvalue crossings that help preserve their shapes and the parallelism that reveals possible symmetry; a more systematic procedure based on eigenvector comparison (as opposed to eigenvalue comparison) works well for one-target scenarios, but breaks down in multitarget cases where there are many more decay curves crossing each other. Again, the number of sources would be estimated correctly, but potentially important information given by the decay shape would be lost.

Figure 7a shows the eigenvalue decay curves for the configuration consisting of the two TOI at the locations from Figure 3. There are seven above-noise eigenvalue curves, indicating that there are at least two targets in the data. The two sets of crossing decay curves from Figure 3 are visible now as a weighted nonlinear superposition of the individual responses, including the fourth eigenvalue associated with the larger shell. Figure 7b and 7c shows the MSR eigenvalues obtained after sequentially adding the first and second clutter items. Ten eigenvalue curves are above the noise in Figure 7b, revealing the presence of three targets, and 12 curves appear in

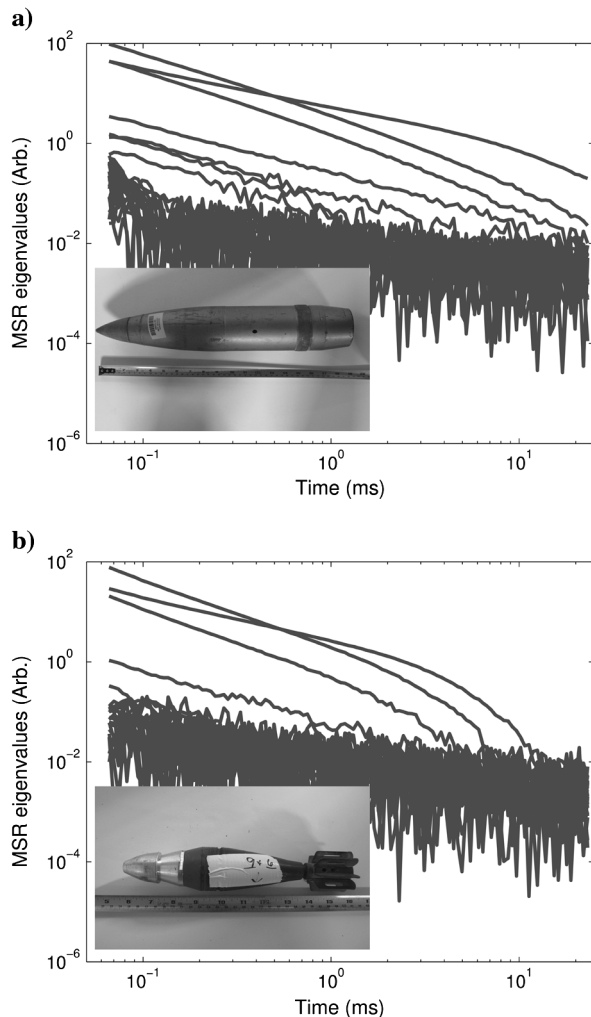


Figure 3. (a) Eigenvalues of the TEMTADS multistatic response matrix for a 105-mm M60 howitzer shell (shown in the inset). (b) Eigenvalues of the TEMTADS multistatic response matrix for a 60-mm M49 mortar round (shown in the inset).

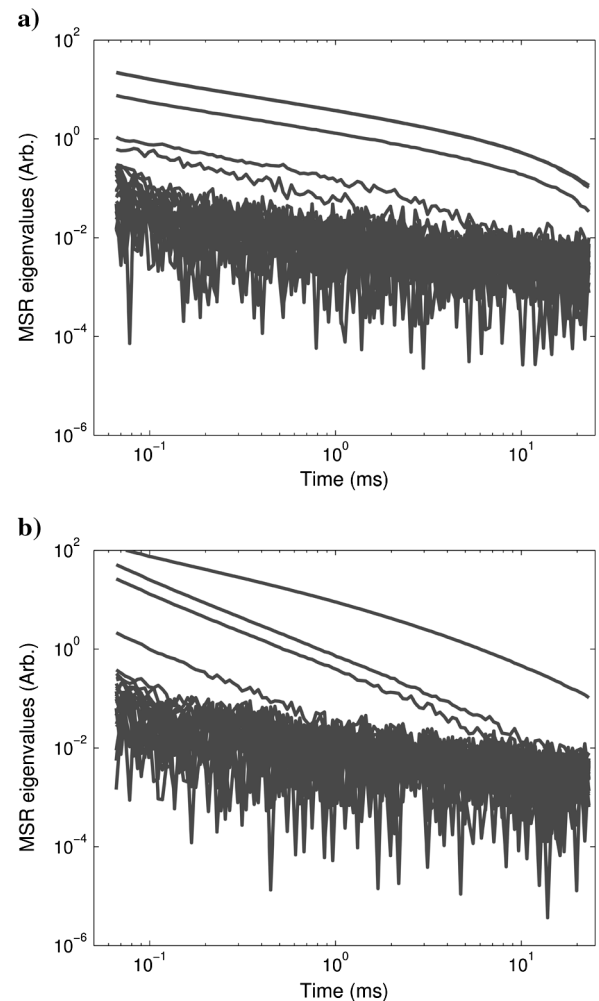


Figure 4. Measured (TEMTADS multistatic response) eigenvalues for an aluminum sphere of diameter 10 cm (a) and a steel prolate spheroid (b) of minor and major axes 4 and 20 cm, respectively.

Figure 7c, showing that the number has increased. The eigenvalue signatures of the original targets can still be discerned, but they are mixed with contributions from clutter items. A scenario with more than six nonzero eigenvalues potentially indicates the presence of a single large shallow target or of several smaller ones and will be routinely dug out when encountered in the field.

Camp Butner blind test

As part of its effort to make UXO remediation faster and more economical, the Environmental Strategic Technology Certification Program (ESTCP) is in the process of administering a series of blind classification tests of increasing realism to measure the progress

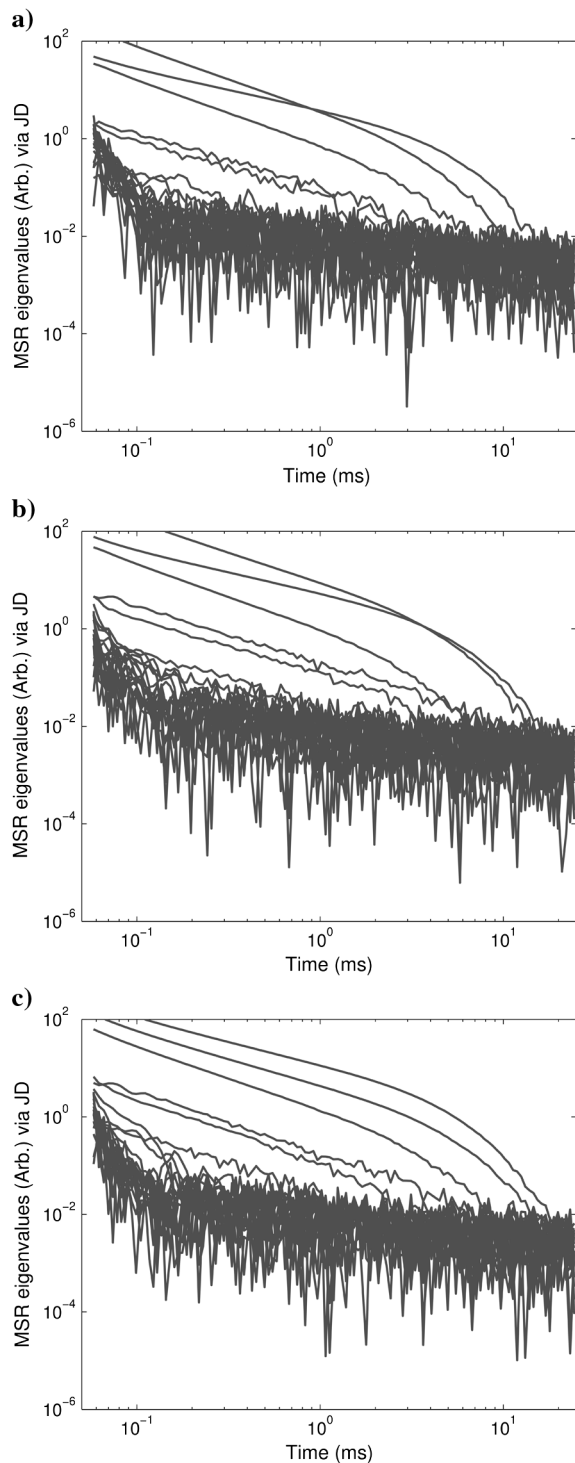


Figure 5. Eigenvalues for the 60-mm round computed using joint diagonalization for three different object locations.

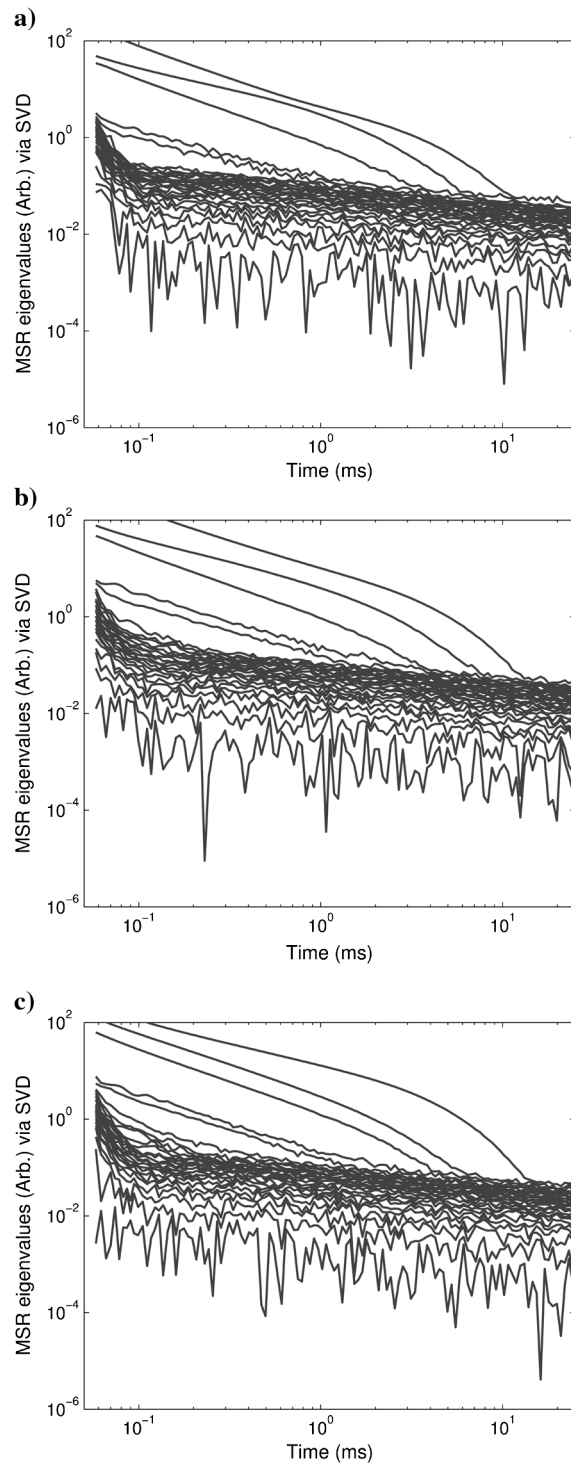


Figure 6. Eigenvalues for the 60-mm round computed using the SVD at each time gate for three different object locations.

made in the development of sensors and inversion and classification algorithms. The first test (Shubitidze et al., 2010c; Fernández et al., 2010), held in 2007 at the former Camp Sibert in Alabama, was relatively straightforward: It was required to discriminate between large, intact 4.2" mortar rounds and smaller explosion byproducts and assorted debris. The data were taken by two first-generation sensors, the EM-61 and EM-63, both developed by Geonics, Inc. There were 150 cells plus 66 for calibration, each one well separated from the others and containing only one target.

The second test (Shamatava et al., 2010; Shubitidze et al., 2010a) was held in 2009 near San Luis Obispo in California. This new test better reflected the wide range of dangerous targets usually present in the field: there were samples of 60-mm mortars, 2.36" rockets (whole and fragments), 81-mm projectiles, and 4.2" mortars; three additional munition types were discovered during the course of the demonstration. Each cell contained an unspecified number of dangerous and/or innocuous targets. The participants were expected not only to identify the UXO, but also to classify them by caliber. The test, moreover, featured a more demanding topography. Magnetometers and commercially available first-generation sensors were used to detect and flag anomalies that were then interrogated more closely by state-of-the-art EMI instruments (TEMTADS, the Berkeley UXO Discriminator, and the Geometrics MetalMapper). The test was at a much larger scale, comprising over 1000 data sets for each instrument.

The third test (SERDP, 2010), on which we concentrate here, took place at the former Camp Butner in North Carolina. Camp Butner functioned as a training ground for infantry divisions and artillery and engineering units during World War II. A large variety of munitions were reportedly used there; at the test site, the targets of interest consisted mostly of 37-mm projectiles (with and without a copper driving band) and 105-mm howitzer shells and HEAT rounds. The clutter items were typical explosion byproducts, such as partial shells and fuzes, along with smaller shrapnel and nonordnance metallic debris. Many of the fragments were similar in size and wall thickness to the 37-mm projectiles (Andrews et al., 2011). The test started with an exploratory cart-based survey using the Geonics EM-61 sensor. The cells in which the EM-61 data indicated the presence of an anomaly (with one or more metallic targets) were then subjected to cued examination with TEMTADS. A total of 2291 cells were interrogated, of which 171 corresponded to potentially hazardous targets. The discrimination results obtained by our group are published elsewhere (Cazares et al., 2011). Here, we demonstrate only our usage of JD to estimate numbers of targets and illustrate shape differences.

Figure 8 shows typical examples of the two kinds of 105-mm projectiles found at the site, along with the time-dependent MSR eigenvalues extracted from the cells that contained them. There are three above-noise eigenvalues in each case, revealing the presence of one target. The howitzer shell of Figure 8a (the large TOI in the test-stand experiment described above) is buried 55 cm below ground, whereas the HEAT round in Figure 8b is 62 cm deep. The signal from the latter is weaker because of the greater depth, despite the lower noise level (which, in the case of Camp Butner, varied substantially from cell to cell). The slow decay of the eigenvalues indicates that these are large targets with substantial metal content (Shubitidze et al., 2010b). Two of the eigenvalues are again seen to be roughly parallel, and in the case of the shell, they overlap each other. The behavior of the other (nonparallel) above-threshold

eigenvalue allows preliminary classification of the target. Figure 8c shows the eigenvalue decay curves (computed using both JD and constrained nonlinear optimization, as discussed in Appendix B) for the HEAT round as measured by TEMTADS in the APG test

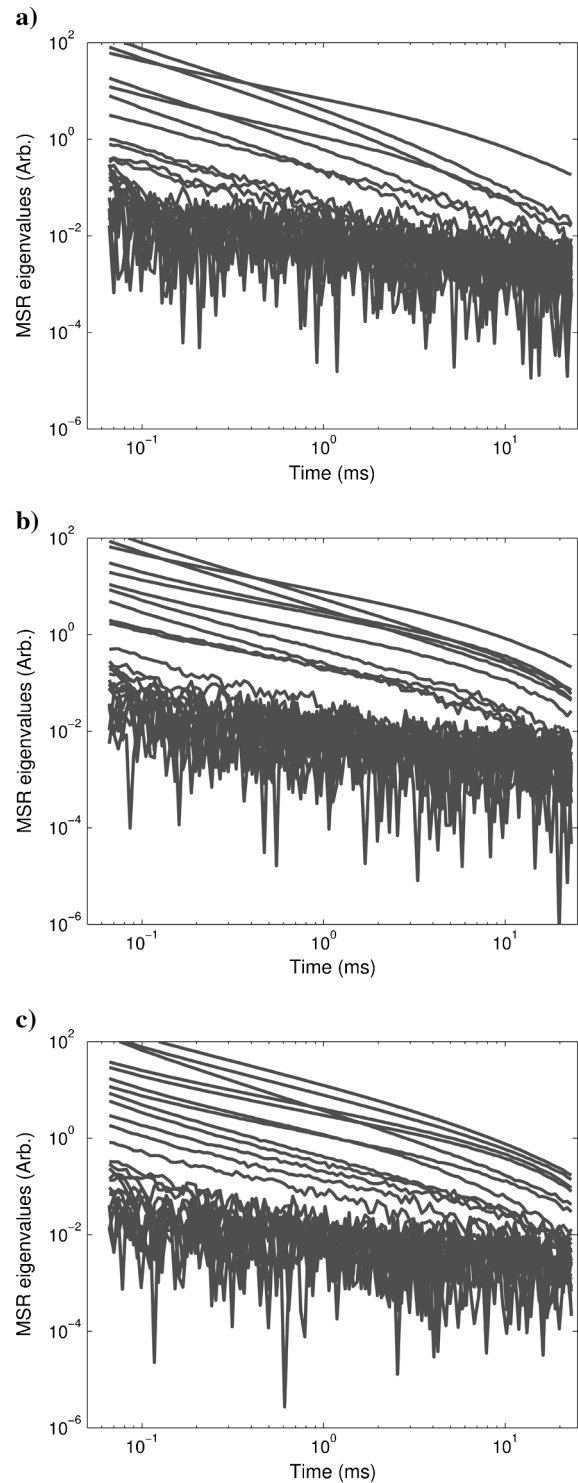


Figure 7. MSR eigenvalues of the test-stand measurements as the munitions of Figure 3 are placed together (a) and then joined by the sphere (b) and by the sphere and spheroid (c) of Figure 4.

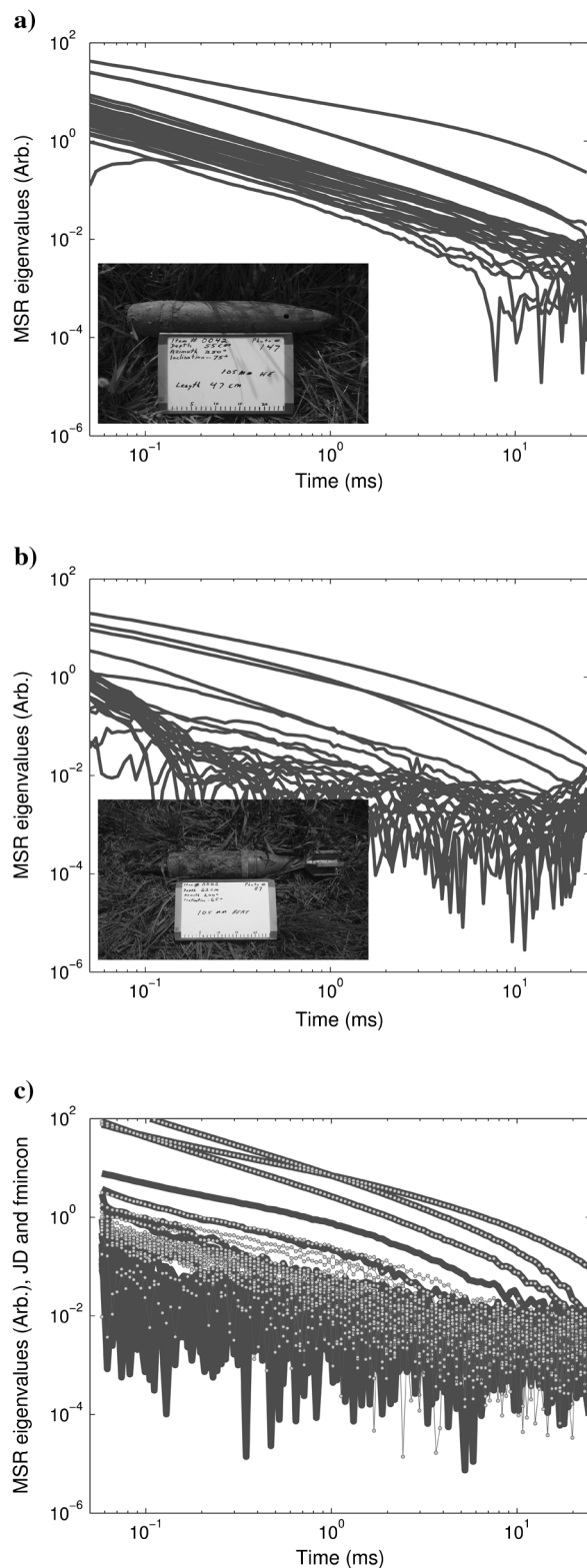


Figure 8. (a) MSR eigenvalues for Camp Butner Cell 42, which contained a 105-mm HE shell buried at a depth of 55 cm. (b) MSR eigenvalues for Camp Butner Cell 62, containing a 105-mm HEAT round buried at 62 cm. (c) MSR eigenvalues for a 105-mm HEAT round placed 53 cm below TEMTADS in the test stand, computed using JD (solid lines) and nonlinear constrained optimization (dots).

stand of the previous section; the munition was 53 cm below the sensor center in that case. The time decay in Figure 8b resembles this measurement more than it does the other cell.

Typical instances of the other Camp Butner TOI, the two different kinds of 37-mm projectiles, are shown along with their time-dependent eigenvalues in Figure 9. The signal in Figure 9a is strong and distinct, reflecting the shallowness of the target (it is only 8 cm deep). The copper driving band, with its high conductivity, influences the signal by retarding its decay. The signal in Figure 9b is much weaker, as the target is at a larger depth, but it has three time-dependent eigenvalues that are distinct from the noise, whose level is similar to that of Figure 9a, through the whole decay.

Figure 10a depicts the result of running JD on a cell that contained a fuze and a small detonation fragment, both located 16 cm below the surface, whereas Figure 10b does the same for a single fuze buried almost twice as deep at 28 cm. In both cases, only three eigenvalue decay curves are above the noise threshold, indicating that the targets in each cell can be represented by a single source. The JD analysis in Figure 10a case fails to identify the small

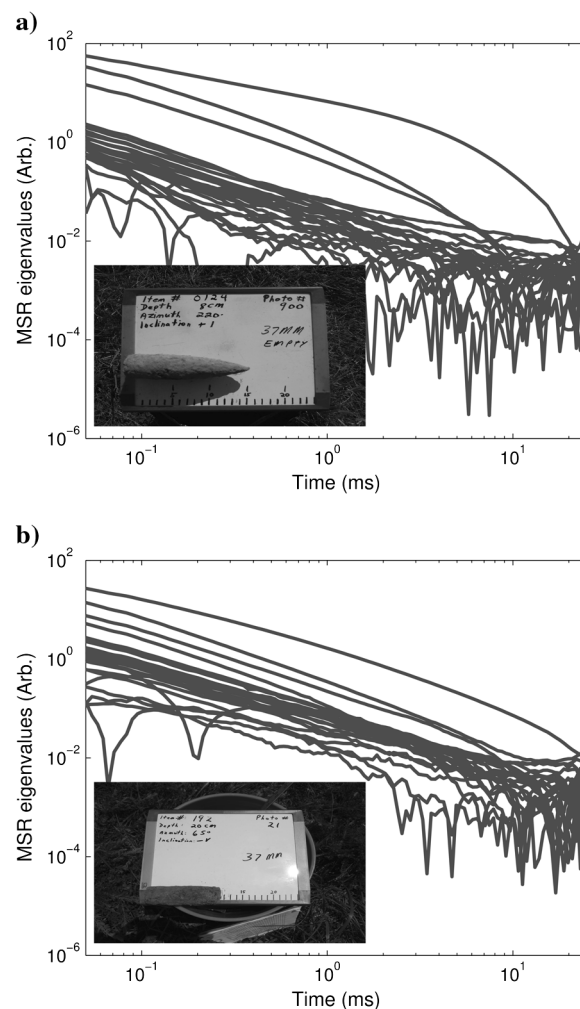


Figure 9. (a) MSR eigenvalues for Camp Butner Cell 124, with one kind of 37-mm projectile at 8 cm below ground. (b) MSR eigenvalues for Camp Butner Cell 192, which contained the other kind of 37-mm projectile, this one at a depth of 20 cm.

fragment, which was located close to the fuze. In Figure 10b, there are still three dominant eigenvalues, but the low signal-to-noise ratio makes them barely discernible. The shape information given by JD was crucial in helping to identify this target correctly. Here, as in all real-world situations, the noise is due simultaneously to the ground, which can be magnetically responsive or wet (or both), to the sensor, and to objects too small or distant to produce detectable individual signals but whose collective response may be significant. Again, it is seen that the MSR eigenvalues mix positional information with intrinsic response: small, shallow targets and large, deep objects produce time-dependent eigenvalues of comparable magnitudes.

In Figure 11, we have a large, shallow sample of “cultural” (i.e., not-ordnance-related) debris: a plowshare with depth of only 7 cm. The eigenvalues are quite large, as expected, but decay very fast in time, indicating that this is not a TOI. The final two figures correspond to multitarget scenarios. In Figure 12a, we have the extracted eigenvalues corresponding to a set of fragments of a 155-mm munition buried at a depth of 50 cm. Two sources suffice to describe the

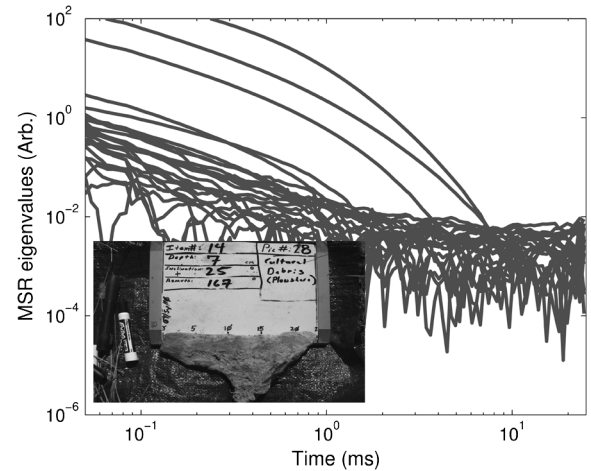


Figure 11. MSR eigenvalues for Camp Butner Cell 14, with a sizable plowshare buried at 7 cm.

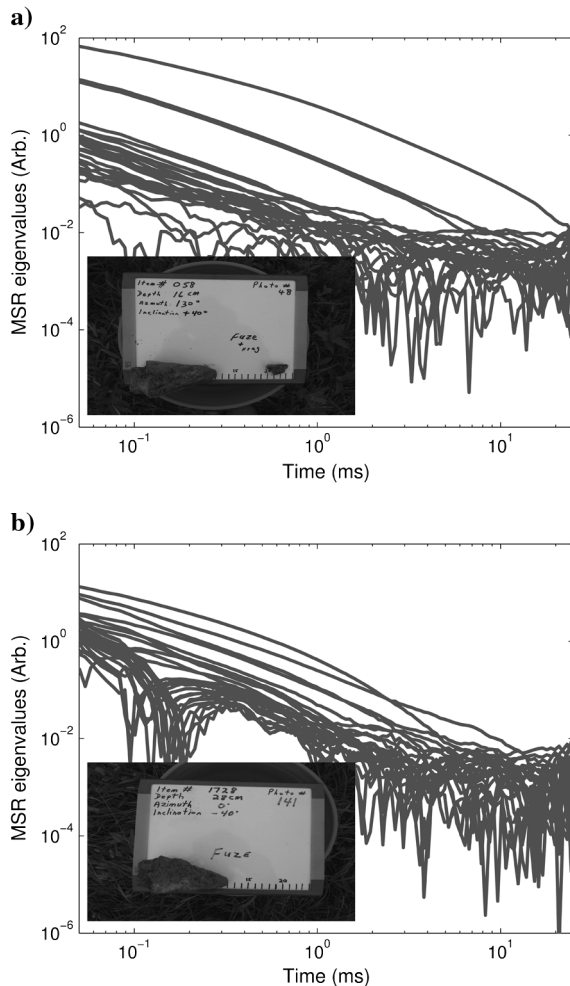


Figure 10. (a) MSR eigenvalues for Camp Butner Cell 58, which contained two explosion byproducts, a fuze and a shrapnel fragment, at a depth of 16 cm. (b) MSR eigenvalues for Camp Butner Cell 1728, which contained another fuze (buried 28 cm below ground).

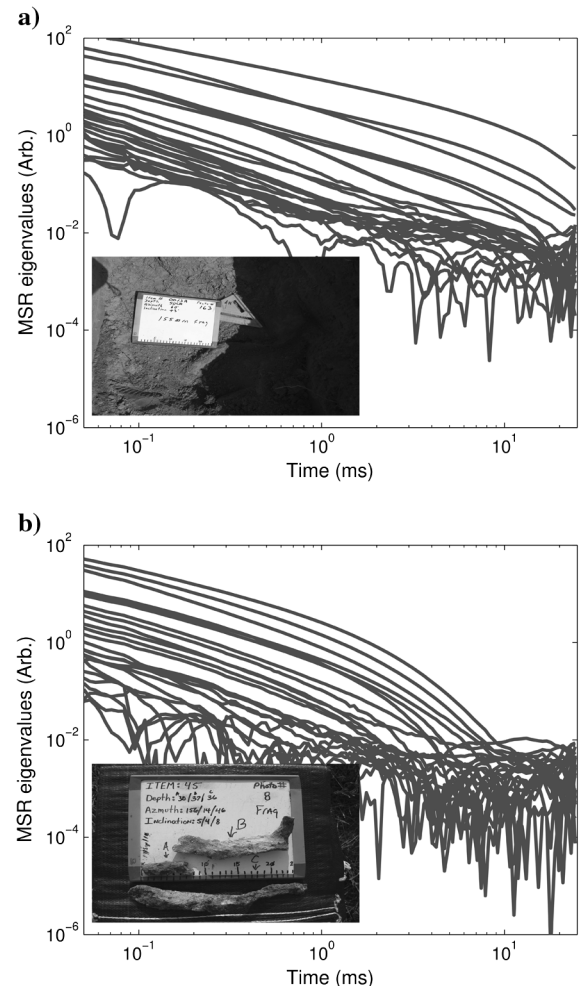


Figure 12. (a) MSR eigenvalues for Camp Butner Cell 13, containing fragments of a 155-mm projectile, buried 50 cm below the ground. (b) MSR eigenvalues for Camp Butner Cell 45, containing numerous fragments, buried at several depths, of a munition that exploded.

objects. Figure 12b depicts the contents and data of a veritable multitarget cell, with several explosion byproducts at a wide assortment of depths. The resulting eigenvalue map can immediately alert operators that there may be several potentially dangerous targets interred below and warn analysts from the outset that any inversion to be performed must involve a forward model that assumes many targets. (Methods to transmit this information could be incorporated into the sensor, and those cells will always be dug out.)

The results of the Camp Butner blind test were scored independently by the Institute for Defense Analyses (Cazares et al., 2011; SERDP, 2011). We correctly characterized all of the 2291 anomalies, each containing at least one target, for which data were provided. All of the 171 potentially dangerous targets were identified as such and also classified by caliber, and our algorithms moreover discriminated between the two kinds of 37-mm projectiles and distinguished the 105-mm HEAT rounds from the other 105-mm shells. We asked for 116 targets to be dug before we were sure that we had identified all the TOI; in contrast, the best analysis using the dipole model required 63 extra digs to reach that level, whereas other procedures needed many more false alarms to be unearthed and in some cases failed to identify UXO (Cazares et al., 2011). One of the stated objectives of the Camp Butner test was to “pave [...] the way for reduced costs and an accelerated timeline to remediate munitions-contaminated sites throughout the nation” (SERDP, 2010). The success of our procedure gives an idea of the progress that has been made toward fulfilling this aim.

CONCLUSION

In this paper, we applied a procedure based on joint diagonalization that provides a fast and reliable inversion-free estimate of the number of targets buried under an EMI sensor. The number of targets can then be input into multitarget inversion procedures, which work much faster and more reliably when given this information. The eigenvalue decay curves found by JD have amplitudes that depend on the location and orientation of the targets, but their shapes, including the appearance of parallel curves for cylindrically symmetric targets, are independent of those particulars. We reiterate that the JD procedure cannot replace inversion, which is still necessary because the depths at which the targets are buried must be known so they can be dug out safely; better knowledge of the locations, moreover, allows better determination of the intrinsic signatures of the targets and consequently more robust and reliable identification and classification.

The JD technique has several other potential uses, which we have started to pursue. It could be used, for example, to remove noise from data by removing the smaller extracted eigenvalues and their corresponding eigenvectors. At the other end, removing the larger eigenvalues and eigenvectors could make it possible to resolve smaller or deeply buried objects. For these applications, it is critical to associate each eigenvalue with its eigenvector unambiguously. In addition, a JD analysis performed in the field can immediately alert data collectors about the noise level, which can then be adjusted by having TEMTADS sample signals for a longer time.

Our aim has been to introduce the JD algorithm and its application to a particular sensor, the TEMTADS array, whose design features make the JD implementation particularly transparent. We have adapted the JD technique to other EMI instruments — the Geometrics MetalMapper and a 2 × 2 portable version of

TEMTADS — and, in the future, we will present the results obtained for blind tests carried out with these tools.

ACKNOWLEDGMENTS

This work was supported by the Strategic Environmental Research and Development Program (SERDP) through Projects MR-1572 and MR-1664 and by the Environmental Strategic Technology Certification Program through Project MR-201101. The authors would like to thank Dan Steinhurst of Nova Research, Inc. for taking the test-stand data.

APPENDIX A

SIMPLIFIED MODEL OF THE MSR MATRIX

We consider an idealized version of TEMTADS consisting of a 5×5 array of vertical dipoles of unit moment $\hat{\mathbf{z}}$ — corresponding to a combination of unit current and unit area — each of which at a given time gate transmits a primary field

$$\begin{aligned} \mathbf{H}^{\text{pr}} &= \frac{1}{4\pi R^5} [3(\hat{\mathbf{z}} \cdot \mathbf{R})\mathbf{R} - \hat{\mathbf{z}}R^2] \\ &= \frac{3ZX}{4\pi R^5} \hat{\mathbf{x}} + \frac{3ZY}{4\pi R^5} \hat{\mathbf{y}} + \frac{3Z^2 - R^2}{4\pi R^5} \hat{\mathbf{z}}, \end{aligned} \quad (\text{A-1})$$

where $\mathbf{R} \equiv X\hat{\mathbf{x}} + Y\hat{\mathbf{y}} + Z\hat{\mathbf{z}} = \mathbf{r} - \mathbf{r}_t$, \mathbf{r} is an observation point, and \mathbf{r}_t is the location of the transmitter. Each TEMTADS dipole receives from a buried source a response \mathbf{H}^{sc} whose z -component reads

$$\begin{aligned} H_z^{\text{sc}} &= \frac{1}{4\pi R^5} (3(\mathbf{m} \cdot \mathbf{R})\mathbf{R} \cdot \hat{\mathbf{z}} - \mathbf{m} \cdot \hat{\mathbf{z}}R^2) \\ &= \frac{1}{4\pi R^5} [3(\hat{\mathbf{z}} \cdot \mathbf{R})\mathbf{R} - \hat{\mathbf{z}}R^2] \cdot \mathbf{m}, \end{aligned} \quad (\text{A-2})$$

where now $\mathbf{R} = \mathbf{r}_r - \mathbf{r}$ with \mathbf{r}_r the location of the receiver. Note that the expressions in square brackets in equations A-1 and A-2 coincide if and only if the (infinitesimal) transmitters and receivers are colocated, as is the case with TEMTADS. The moment \mathbf{m} induced in the responding source is given as in equation 4. The MSR matrix for the transmitter/receiver array is constructed by assembling N_t samples of equation A-1 for the transmitted field and N_r samples of the received response A-2, thus forming the Green tensors

$$\mathbf{G}^{\text{pr}} = \begin{bmatrix} \frac{3ZX}{4\pi R^5} & \frac{3ZY}{4\pi R^5} & \frac{3Z^2 - R^2}{4\pi R^5} \end{bmatrix} \in \mathbb{R}^{N_t \times 3}, \quad (\text{A-3})$$

$$\mathbf{G}^{\text{sc}} = \begin{bmatrix} \frac{3ZX}{4\pi R^5} & \frac{3ZY}{4\pi R^5} & \frac{3Z^2 - R^2}{4\pi R^5} \end{bmatrix} \in \mathbb{R}^{N_r \times 3}. \quad (\text{A-4})$$

The measured secondary signal given in equation 1 is

$$\mathbf{S} = \mathbf{G}^{\text{sc}}(\mathbf{U}\mathbf{\Lambda}\mathbf{U}^T)(\mathbf{G}^{\text{pr}})^T = (\mathbf{G}^{\text{sc}}\mathbf{U})\mathbf{\Lambda}(\mathbf{G}^{\text{pr}}\mathbf{U})^T, \quad (\text{A-5})$$

where \mathbf{U} and $\mathbf{\Lambda}$ are 3×3 matrices.

We can use this simplified model to provide a plausibility argument for one of our findings: Targets with cylindrical or spherical symmetry have a pair of eigenvalues whose log-log decay curves look parallel (i.e., there is a constant ratio between the two). Take \mathbf{G}^{pr} and \mathbf{G}^{sc} to be identical, as the geometry above allows, and

consider a 2×2 sensor array such that the Tx/Rx pairs are located at $\mathbf{r}_i = \ell(\pm \hat{\mathbf{x}} \pm \hat{\mathbf{y}})$, where $\ell = 0.20$ cm in the case of TEMTADS. Suppose the target is a dipole buried at depth z_0 below the center of the array and characterized by the cylindrically symmetric polarizability tensor $\mathbf{\Lambda} = \beta \text{diag}(1, 1, \lambda)$. Ordering the Tx/Rx dipoles clockwise from the top left of the array, we obtain the MSR matrix

$$\mathbf{S} = \beta \left(\frac{3z_0\ell}{4\pi R^5} \right)^2 \begin{bmatrix} -1 & 1 & \kappa \\ 1 & 1 & \kappa \\ 1 & -1 & \kappa \\ -1 & -1 & \kappa \end{bmatrix} \mathbf{U} \mathbf{\Lambda} \mathbf{U}^T \begin{bmatrix} -1 & 1 & 1 & -1 \\ 1 & 1 & -1 & -1 \\ \kappa & \kappa & \kappa & \kappa \end{bmatrix}, \quad (\text{A-6})$$

where we have introduced the dimensionless parameter

$$\kappa = \frac{3z_0^2 - R^2}{3z_0\ell} = \frac{2}{3} \left(\frac{z_0}{\ell} - \frac{\ell}{z_0} \right), \quad \text{which implies} \quad z_0 = \frac{\ell}{4} (3\kappa + \sqrt{9\kappa^2 + 16}). \quad (\text{A-7})$$

If the target is a horizontal dipole, the polarizability tensor is $\mathbf{U} \mathbf{\Lambda} \mathbf{U}^T = \beta \text{diag}(\lambda, 1, 1)$ and the MSR matrix A-6 becomes

$$\mathbf{S} = \beta \left(\frac{3z_0\ell}{4\pi R^5} \right)^2 \times \begin{bmatrix} (1+\lambda) + \kappa^2 & (1-\lambda) + \kappa^2 & -(1+\lambda) + \kappa^2 & -(1-\lambda) + \kappa^2 \\ (1-\lambda) + \kappa^2 & (1+\lambda) + \kappa^2 & -(1-\lambda) + \kappa^2 & -(1+\lambda) + \kappa^2 \\ -(1+\lambda) + \kappa^2 & -(1-\lambda) + \kappa^2 & (1+\lambda) + \kappa^2 & (1-\lambda) + \kappa^2 \\ -(1-\lambda) + \kappa^2 & -(1+\lambda) + \kappa^2 & (1-\lambda) + \kappa^2 & (1+\lambda) + \kappa^2 \end{bmatrix}. \quad (\text{A-8})$$

The eigenvalues of this 4×4 matrix are 0, 4, $4\kappa^2$, and 4λ . One eigenvalue vanishes, confirming that there is only one target. The nonzero eigenvalues are in general not degenerate, even for highly symmetric configurations. (The eigenvalues coincide for the special case $z_0 = 2\ell$.) On the other hand, there is a constant ratio κ^2 between two of the eigenvalues, allowing extraction of the extrinsic depth z_0 through the definition in equation A-7. (Cylindrical symmetry is important here; if $\mathbf{\Lambda} = \beta \text{diag}(1, \mu, \lambda)$, the MSR eigenvalues become 0, $4\kappa^2$, 4μ , and 4λ , with all significant ratios now time-dependent.) This undertaking quickly becomes nontrivial: for example, when the target is vertical, the MSR eigenvalues are 0, 4, 4, and $4\lambda\kappa^2$; the intrinsic and extrinsic features are coupled. The analysis is further complicated if the target is displaced from the center of the Tx/Rx array or has another orientation, or if the Tx/Rx array is larger than 2×2 .

APPENDIX B

ALGORITHM FOR JOINT DIAGONALIZATION

The joint diagonalization algorithm we use (Flury and Gautschi, 1986; Cardoso and Souloumiac, 1996; Belouchrani et al., 1997) is a generalization of Jacobi's procedure to find the eigenvalues of a single matrix. Formally, we solve the optimization problem

$$\begin{aligned} \min_{\mathbf{V}} \quad & \frac{1}{2} \sum_{q=1}^N \sum_{i \neq j} ([\mathbf{V} \mathbf{A}(t_q) \mathbf{V}^T]_{ij})^2, \\ \text{s.t.} \quad & \mathbf{V}^T \mathbf{V} = \mathbf{I} \end{aligned} \quad (\text{B-1})$$

where \mathbf{I} is the identity matrix. We accomplish this by making repeated Givens-Jacobi similarity transformations designed to gradually accumulate the "content" of the matrices on their diagonals until a certain tolerance level is reached. The transformations are of the form $\mathbf{A}(t_q) \rightarrow \mathbf{A}'(t_q) = \mathbf{V}_{rs} \mathbf{A}(t_q) \mathbf{V}_{rs}^T$, with the matrix \mathbf{V}_{rs} being the identity but with the four elements V_{rr} , V_{rs} , V_{sr} , and V_{ss} replaced by the 2D rotation array

$$\begin{bmatrix} \cos \phi_{rs} & \sin \phi_{rs} \\ -\sin \phi_{rs} & \cos \phi_{rs} \end{bmatrix}, \quad \tan 2\phi_{rs} = \frac{f_{rs}}{n_{rs} + \sqrt{f_{rs}^2 + n_{rs}^2}}, \quad (\text{B-2})$$

where

$$n_{rs} = \sum_q \{ [a_{rr}(t_q) - a_{ss}(t_q)]^2 - [a_{rs}(t_q) + a_{sr}(t_q)]^2 \}, \quad (\text{B-3})$$

$$f_{rs} = 2 \sum_q [a_{rr}(t_q) - a_{ss}(t_q)][a_{rs}(t_q) + a_{sr}(t_q)]. \quad (\text{B-4})$$

The indices are swept systematically and the procedure is repeated until convergence is reached. The computational burden is equivalent to that of diagonalizing the matrices one by one. The resulting eigenvalues and eigenvectors are all real because all the MSR matrices are symmetric.

We have also solved the nonlinear constrained optimization problem B-1 directly using sequential quadratic programming as implemented in the function *fmincon* of the Matlab Optimization Toolbox (The MathWorks, 2006). This procedure unsurprisingly takes a longer time to run than the Givens-Jacobi algorithm sketched above. The two procedures gave equivalent results in all cases we tried; Figure 8c shows an example.

REFERENCES

- The MathWorks, 2006, Optimization Toolbox user's guide, Version 3.
- Andrews, A., H. H. Nelson, and K. Kaye, 2011, ESTCP pilot program: Classification approaches in munitions response, Camp Butner, North Carolina, <http://serdp-estcp.org/content/download/10723/136271/version/4/file/Butner+Demonstration+Program+Office+Final+Report+July.pdf>, accessed 12 April 2012.
- Aster, R. C., B. Borchers, and C. H. Thurber, 2005, Parameter estimation and inverse problems: Elsevier, Inc.
- Barrow, B. J., and H. H. Nelson, 2001, Model-based characterization of electromagnetic induction signatures obtained with the MTADS electromagnetic array: IEEE Transactions on Geoscience and Remote Sensing, **39**, 1279–1285, doi: [10.1109/36.927450](https://doi.org/10.1109/36.927450).
- Bell, T. H., B. J. Barrow, and J. T. Miller, 2001, Subsurface discrimination using electromagnetic induction sensors: IEEE Transactions on Geoscience and Remote Sensing, **39**, 1286–1293, doi: [10.1109/36.927451](https://doi.org/10.1109/36.927451).
- Belouchrani, A., K. Abed-Meraim, J.-F. Cardoso, and E. Moulines, 1997, A blind source separation technique using second-order statistics: IEEE Transactions on Signal Processing, **45**, no. 2, 434–444, doi: [10.1109/78.554307](https://doi.org/10.1109/78.554307).
- Bogdanov, F. G., D. D. Karkashadze, and R. S. Zaridze, 1999, The method of auxiliary sources in electromagnetic scattering problems, in T. Wriedt, ed., Generalized multipole techniques for electromagnetic and light scattering: Elsevier Science, 143–172.
- Cardoso, J.-F., and A. Souloumiac, 1996, Jacobi angles for simultaneous diagonalization: SIAM Journal on Matrix Analysis and Applications, **17**, no. 1, 161–164, doi: [10.1137/S0895479893259546](https://doi.org/10.1137/S0895479893259546).
- Cazares, S., M. Tuley, and E. Ayers, 2011, The UXO classification demonstration at former Camp Butner, NC, <http://serdp-estcp.org/content/>

- [download/12777/151554/version/1/file/IDA_Camp+Butner_Report_1-13.pdf](#), accessed 9 April 2012.
- Comon, P., 1994, Independent component analysis, a new concept?: *Signal Processing*, **36**, no. 3, 287–314, doi: [10.1016/0165-1684\(94\)90029-9](#).
- Das, Y., J. E. McFee, J. Toews, and G. C. Stuart, 1990, Analysis of an electromagnetic induction detector for real-time location of buried objects: *IEEE Transactions on Geoscience and Remote Sensing*, **28**, 278–288, doi: [10.1109/36.54354](#).
- Everett, M. E., 2012, Theoretical developments in electromagnetic induction geophysics with selected applications in the near surface: *Surveys in Geophysics*, **33**, 29–63, doi: [10.1007/s10712-011-9138-y](#).
- Fernández, J. P., B. E. Barrowes, T. M. Grzegorzczak, N. Lhomme, K. O'Neill, and F. Shubitidze, 2011, A man-portable vector sensor for identification of unexploded ordnance: *IEEE Sensors Journal*, **11**, no. 10, 2542–2555, doi: [10.1109/JSEN.2011.2118200](#).
- Fernández, J. P., B. E. Barrowes, K. O'Neill, I. Shamatava, and F. Shubitidze, 2010, Realistic subsurface anomaly discrimination using electromagnetic induction and an SVM classifier: *EURASIP Journal on Advances in Signal Processing*, **2010**, 305890, doi: [10.1155/2010/305890](#).
- Flury, B. N., and W. Gautschi, 1986, An algorithm for simultaneous orthogonal transformation of several positive definite symmetric matrices to nearly diagonal form: *SIAM Journal on Scientific and Statistical Computing*, **7**, no. 1, 169–184, doi: [10.1137/0907013](#).
- Grzegorzczak, T. M., B. E. Barrowes, F. Shubitidze, J. P. Fernández, and K. O'Neill, 2011, Simultaneous identification of multiple unexploded ordnance using electromagnetic induction sensors: *IEEE Transactions on Geoscience and Remote Sensing*, **49**, 2507–2517, doi: [10.1109/TGRS.2011.2108302](#).
- Harmeling, S., A. Ziehe, M. Kawanabe, and K.-R. Müller, 2003, Kernel-based nonlinear blind source separation: *Neural Computation*, **15**, no. 5, 1089–1124, doi: [10.1162/089976603765202677](#).
- Karkashadze, D., J. P. Fernández, and F. Shubitidze, 2009, Scatterer localization using a left-handed medium: *Optics Express*, **17**, no. 12, 9904–9917, doi: [10.1364/OE.17.009904](#).
- Machara, T., and K. Murota, 2011, Simultaneous singular value decomposition: *Linear Algebra and Its Applications*, **435**, no. 1, 106–116, doi: [10.1016/j.laa.2011.01.007](#).
- Moyes, R., R. Lloyd, and R. McGrath, 2002, Explosive remnants of war: Unexploded ordnance and post-conflict communities: *Landmine Action*.
- Pasion, L. R., and D. W. Oldenburg, 2001, A discrimination algorithm for UXO using time-domain electromagnetics: *Journal of Environmental and Engineering Geophysics*, **6**, no. 2, 91–102, doi: [10.4133/JEEG6.2.91](#).
- SERDP, 2010, Success classifying small munitions at Camp Butner, <http://serdp-estcp.org/News-and-Events/In-the-Spotlight-Archive/Success-Classifying-Small-Munitions-at-Camp-Butner>, accessed 22 February 2012.
- SERDP, 2011, Advanced signal processing for UXO discrimination, <http://www.serdp.org/News-and-Events/In-the-Spotlight/Advanced-Signal-Processing-for-UXO-Discrimination>, accessed 22 February 2012.
- Shamatava, I., F. Shubitidze, J. P. Fernández, B. E. Barrowes, K. A. O'Neill, and T. M. Grzegorzczak, 2010, SLO blind data set inversion and classification using physically complete models: *Proceedings of SPIE*, **7664**, 766404, doi: [10.1117/12.850621](#).
- Shubitidze, F., J. P. Fernández, I. Shamatava, B. E. Barrowes, K. A. O'Neill, and T. M. Grzegorzczak, 2010a, Comparison of the physically complete model with a simple dipole model for UXO detection and discrimination: *Proceedings of SPIE*, **7664**, 766408, doi: [10.1117/12.850654](#).
- Shubitidze, F., J. P. Fernández, I. Shamatava, L. R. Pasion, B. E. Barrowes, and K. O'Neill, 2010b, Application of the normalized surface magnetic source model to a blind unexploded ordnance discrimination test: *ACES Journal*, **25**, no. 1, 89–98.
- Shubitidze, F., D. Karkashadze, J. P. Fernández, B. E. Barrowes, K. O'Neill, T. Grzegorzczak, and I. Shamatava, 2010c, Applying a volume dipole distribution model to next-generation sensor data for multi-object data inversion and discrimination: *Proceedings of SPIE*, **7664**, 766406, doi: [10.1117/12.850651](#).
- Smith, J. T., and L. F. Morrison, 2004, Estimating equivalent dipole polarizabilities for the inductive response of isolated conductive bodies: *IEEE Transactions on Geoscience and Remote Sensing*, **42**, 1208–1214, doi: [10.1109/TGRS.2004.826789](#).
- Song, L.-P., D. W. Oldenburg, L. R. Pasion, and S. D. Billings, 2009, Transient electromagnetic inversion for multiple targets: *Proceedings of SPIE*, **7303**, 73030R, doi: [10.1117/12.818769](#).
- Song, L.-P., L. R. Pasion, S. D. Billings, and D. W. Oldenburg, 2011, Non-linear inversion for multiple objects in transient electromagnetic induction sensing of unexploded ordnance: Technique and applications: *IEEE Transactions on Geoscience and Remote Sensing*, **49**, 4007–4020, doi: [10.1109/TGRS.2011.2132138](#).
- Steinhurst, D. A., G. R. Harbaugh, J. B. Kingdon, T. Furuya, D. A. Keiswetter, and D. C. George, 2010, EMI array for cued UXO discrimination, ESTCP project MM-0601 final report, <http://www.serdp.org/Program-Areas/Munitions-Response/Land/Sensors/MR-200601/MR-200601>, accessed 22 September 2011.
- Tarokh, A. B., E. L. Miller, I. J. Won, and H. Huang, 2004, Statistical classification of buried objects from spatially sampled time or frequency domain electromagnetic induction data: *Radio Science*, **39**, RS4S05, doi: [10.1029/2003RS002951](#).
- Zhang, Y., L. Collins, H. Yu, C. E. Baum, and L. Carin, 2003, Sensing of unexploded ordnance with magnetometer and induction data: Theory and signal processing: *IEEE Transactions on Geoscience and Remote Sensing*, **41**, 1005–1015, doi: [10.1109/TGRS.2003.810922](#).